Available online at www.sciencedirect.com
SCIENCE DIRECT®
Journal of Nuclear Materials 352 (2006) 126–135
journal of nuclear materials
www.elsevier.com/locate/jnucmat

Feeling defects in Zircaloy by extended X-ray absorption fine structure and muon spin relaxation analyses

C. Degueldre [a,*], St. Conradson [b], A. Amato [a], E. Campitelli [a]

[a] *LWV&LMU, Paul Scherrer Institut, 5232 Villigen, Switzerland*
[b] *Los Alamos National Laboratory, Los Alamos, NM, United States*

Abstract

The defects generated by plastic deformation of Zircaloy by cold rolling and the resulting sub-nanoscopic environment are investigated using results provided by extended X-ray fine structure (EXAFS) spectroscopy and muon spin relaxation (MuSR) analysis. EXAFS allows to visualizing the atomic environment as a function of the induced strain. The defects are deduced from the next neighbour number determined shell per shell by the EXAFS analysis. An additional dimension is added with the study of muon properties in the material, namely the possibility of examining different states of the defect centres over the sub-nanometric scale. Muon spin relaxation analysis provides information about the local order around the muon and about possible muon diffusion in the material. Combining these techniques allows to completing the complex picture yields by the defect creation yielded by plastic deformation due to cold rolling in Zircaloy.

PACS: 61.10.Ht; 76.75.+i

1. Introduction

Since Zircaloy (Zry2 in this study) cladding form a barrier between the nuclear fuel and the coolant, the study of Zry structure is crucial in nuclear industry. At the laboratory level, numerous intensive programs concern the study of defects as well as their formation. This study takes place in the frame of the CMB (core material behaviour) project, whose focus is the characterization and evaluation of the performance of nuclear core materials. Zircaloy nuclear fuel claddings are subjected to deterioration during service exposure. Basic understanding of the damage mechanisms is therefore mandatory for a lifetime assessment of the claddings under normal operating and accident conditions. The objectives of the project are to understand the mechanisms of degradation with respect to microstructural, mechanical, and corrosion performance [1].

Like magnesium and other elements at room temperature such as: beryllium, titanium, cobalt and zinc, α-zirconium is hexagonal close-packed (hcp) and its extended structure space group is $P6_3/mmc$ (194). Its hexagonal lattice parameters are: $a = b = 323.2$ pm, $c = 514.7$ pm, $\alpha = \beta =$

* Corresponding author. Tel.: +41 56 3104176; fax: +41 56 3104595.
E-mail address: claude.degueldre@psi.ch (C. Degueldre).

0022-3115/$ - see front matter © 2006 Elsevier B.V. All rights reserved.
doi:10.1016/j.jnucmat.2006.02.046

90.000° and $\gamma = 120.000°$ [2]. With tin, Zry2 forms a solid solution which mechanical properties are versatile for its production.

Cold rolling is a process by which the sheet metal is introduced between rollers and then compressed and squeezed. The amount of strain introduced determines the hardness and other material properties of the finished product. Cold rolling is generally used for its advantages, namely: good dimensional accuracy and surface finish. Here, it introduces dislocations that are considered somewhat to simulate irradiation microstructure. Cold rolling of zirconium was recently studied by Dinda et al. [3] characterising the samples sequentially rolled and folded by TEM and XRD providing information at the nanoscopic level. Kumar et al. [4] explained absence of texture development in cold rolled two-phase zirconium – 2.5 wt% niobium alloy and Kapoor et al. [5] investigated by X-ray measurement the near surface residual stress in textured cold-worked zirconium – 2.5% niobium pressure tube material.

A sub-nanoscopic picture of atoms environment in Zircaloy is consequently complementary. It may be performed by EXAFS, which would be able to visualize the atom distributions in a radial way but not directly the vacancies in the lattice. The latter features are however deduced from the complex and detailed picture provided by the EXAFS analysis. EXAFS has been applied to study hexagonal metals, e.g., Mg, Y and Zn [6]. However, nothing is reported about zirconium or Zircaloy.

An additional dimension is added with the study of muons in the material, namely the possibility of examining trapping centres and/or diffusion of diamagnetic muons. Muon spin relaxation analysis has been successfully used to characterize these features, determining the local structures using stability, mobility and interactions of muons in different materials. In addition, characterization of trapping centres such vacancies may be derived and numerous studies are reported for metals (see, e.g., [7]). Studies were carried for copper, gold, silver, platinum, aluminium, niobium [8] for which muon (μ^+) may be regarded as an isotopic analogue of the proton, with a positive muon replacing the proton. Its mass is however 0.1126 atomic mass unit.

In this study Zry2 samples are studied by EXAFS to compare the defects density and their extension during plastic deformation at increasing intensity; the work is completed by a MuSR study.

2. Theory

2.1. Cold rolling

The samples deformed by cold rolling undergo strains. The deformation strain ($\varepsilon\%$) is simply given by:

$$\varepsilon = 100 \cdot \ln(L_f/L_i), \tag{1}$$

with L_i the initial length of the foil and L_f the final length after rolling.

2.2. X-ray absorption

The Extended X-ray Absorption Fine Structure (EXAFS) region of, μ, the absorption coefficient, extending in the energy scale, E, from around 15–30 eV up to 300–1600 eV past the absorption edge, consists of the absorption modulations, $\chi(k)$ with k the magnitude of the photoelectron wave vector, that are superimposed on the smooth, monotonically decreasing, atomic portion of the absorption, μ_0. The normalised absorption χ may then be reported in k or R space showing EXAFS data as a sum of individual waves due to different types of neighbouring atoms. The modulation of the interferences with the change in X-ray energy and photoelectron wavelength is given by the EXAFS expression

$$\chi(k) = \frac{\mu - \mu_0}{\mu_0} = \sum_{j=1}^{n} \left[\frac{N_j}{k \cdot R_j^2} f_j(\pi, k) \cdot e^{-2k^2 \cdot \sigma_j^2} \cdot e^{(-2R_j/\lambda)} \cdot \sin(2k \cdot R_j + \varphi_j) \right] \tag{2}$$

with $k = \sqrt{2m_e \cdot (E - E_0)/\hbar^2}$, E the X-ray energy, E_0 the ionisation energy, m_e the electron mass, N_j the number of neighbour atoms of the same Z at the same distance R_j from the absorbing atom (shell j), f_j the backscattering per atom function for that shell, σ_j the Debye–Walker factor to account for thermal vibration, φ_j the phase shift and λ the mean free path [9].

Because each shell of neighbour atoms contributes a (modified) sine wave to the total $\chi(k)$, Fourier transformation gives a function whose modulus bears some resemblance to the average partial pair distribution function with respect to the target element, subject to the caveats that (1) the positions of the peaks are at lower distance than the actual absorber–scatterer separations because of the photoelectron phase shift; (2) multiple scattering paths

may produce spectral features that do not correspond to structural ones; and (3) destructive interference between the EXAFS from individual shells or because of a non-Gaussian distribution within a shell can significantly modify and reduce the amplitude of the contribution of a shell of atoms. It is therefore common to present the spectra (both experimental and calculated) as $\chi(R)$ rather than the $\chi(k)$ representation. Even in the single scattering formalism [11] it can be shown that the EXAFS depends on and therefore can be used to determine the absorber-neighbour distance R to within ± 0.01–0.03 Å, the number of neighbours to within ± 10–30%, and the type of neighbour atom to $Z \pm 2$–4, for each resolvable, shell of ordered neighbour atoms out to 3–7 Å, i.e., with precision that easily permits the observation of changes in chemical speciation. Because 'ordered' for EXAFS means with respect to the absorber-neighbour distance and not to the crystal lattice, EXAFS is sensitive to aperiodic local lattice distortions that are invisible to normal, diffraction-based, crystallographic methods when they involve around 10% or more of the atoms. It therefore provides smaller scale information that is complementary to the long range average structures obtained through diffraction analysis. The other advantage of EXAFS is that it is particularly sensitive to changes in the local absorber environments between related materials, e.g., ones with different amounts of strain, in which case the accuracy in determining the difference can be better than the lower limits listed above.

2.3. Muon spectroscopy

The produced muons are implanted one at a time into the sample where they thermalise within a few picoseconds. During its lifetime (half life (τ_μ) 2.2 μs) the muon can diffuse in the material as free muon (μ^+) or possibly as muonium (μ^+–e^-). When the muon undergoes its decay a positron, among others, is produced which is preferentially emitted along the direction of the muon spin at decay time. In practice, it is not the spin of an individual muon, which is followed but the spin of an ensemble of muons. This ensemble is analysed by studying one muon at a time. The obvious exponential reflects the muon live time, while the oscillation is due to the precession of muons in the applied field. The amplitude of this oscillation is a function of the number of counts is termed the asymmetry. The MuSR signal is given by

$$N(t) = N_0 \exp(-t/\tau_\mu)[1 + AG(t)] + B_g, \quad (3)$$

where B_g is a time-independent background, N_0 is a normalization constant, τ_μ is the muon lifetime and the exponential accounts for the muon decay. $AG(t)$ is often called the μSR signal. A is the asymmetry parameter, which will depend on the experimental setup. $G(t)$ reflects the normalized muon–spin S autocorrelation function $G(t) = \langle S \cdot S(0)\rangle / S(0)^2$, which depends on the average value, distribution, and time evolution of the internal fields sensed by the muons, and therefore contains all the physics of the magnetic interactions of the muon inside the sample [10]. The present MuSR measurements were obtained with the so-called transverse-field technique where a weak magnetic field is applied transverse to the initial spin direction. The form and width of the field distribution sensed by the muon is therefore detected by monitoring the decay of the muon polarization (i.e., reflected by the envelope $g(t)$ of the $G(t)$ function).

In metals, the implanted muon comes at rest at an interstitial position and is in a diamagnetic state. After implantation, it may diffuse between interstitial sites and/or towards trapping spaces (defects, vacancies, foreign atoms). By μSR technique, information about the local magnetic field distribution at the muon site can be obtained. Such distribution will be sensitive to the dynamics of the local magnetic moments (such as nuclear moments) and/or of the muon itself. Consequently muon diffusion in metals may be investigated and numerous studies are reported for elemental metals (see, e.g., [11,12]). Alternatively, in dielectrics, part of the implanted muons can capture an electron and form a muonium pseudo-atom. The muonium properties, including the nature of trapping sites and its diffusion, can in turn be studied by μSR, as successfully demonstrated in a variety of studies (for a comprehensive review on muon and muonium diffusion [13]).

3. Experimental

3.1. Material

Zircaloy 2 samples were originally recrystallised for 0.5 h at 600 °C. Zircaloy is in essence a solid substitutional solution of Sn (1.2–1.7 wt%) with a mean grain size of about 10 μm in our case. Oxygen is another alloy element found in solution as an interstitial. Zircaloy also contains smaller amounts of Fe, Cr and Ni in the form of small intra-

Table 1
Composition of the Zircaloy 2

Element	Zr	Sn	O	Fe	Cr	Ni
Fraction (wt%)*	98.55–**98.31**–97.63	1.20–**1.35**–1.70	0.10–**0.12**–0.14	0.07–**0.17**–0.20	0.05–**0.10**–0.15	0.03–**0.05**–0.08
Fraction (at.%)**	99.07–**98.94**–98.69	0.57–**0.64**–0.81	0.35–**0.42**–0.50	–	–	–
Density (g cm^{-3})**	6.50			–		

(Figures: regular for Zry2 and bold for actual sample), note in grey background the secondary phase components; Considering * for 1 metal phase and ** for 2 separate metal phases, ■ values not reported for secondary phases, e.g., $Zr(Fe,Cr)_2$, $Zr_2(Ni,Fe)$.

granular intermetallic precipitates (e.g., $Zr(Fe,Cr)_2$, $Zr_2(Ni,Fe)$). The last ones have very low solubility in the Zr matrix (see Table 1).

The starting recrystallised Zircaloy 2 material was investigated by transmission electron microscopy (TEM) using a Jeol Type 2010 unit. Sample preparation was done electrolytically (60% $HClO_4$, 40% ethanol) in a Struers Tenupol. The recrystallised Zircaloy 2 bright field image, showed equiaxed grains, local dislocation loops and secondary phase particles. The micrograph revealed hexagonal crystals of 10 μm basal lattice. Plastic deformation treatment was performed at room temperature by cold-rolling to yield several increasing strains used for this investigation. The applied strain on Zry2 samples were 10, 20, 50 and 100%.

3.2. X-ray absorption

The samples as metal strips stuck on to an Al sample holder with vacuum grease. The holder was then fastened onto an adapter mounted on the cold finger of a liquid N_2-cooled cryostat that was used to cool the samples to minimize the thermal contribution to the Debye–Waller factors. XAFS measurements were performed at beamline 11–2 of the Stanford Synchrotron Radiation Laboratory, under dedicated synchrotron X-ray production conditions (3.0 GeV e^-, 70–100 mA) [14].

Si (2 2 0) crystals were used to monochromate the beam. Zr K edge spectra from the opaque samples were obtained in the fluorescence mode by monitoring the Kα emission line using 24–30 elements of a multi-element Ge detector array and digital amplifiers. A Pt-coated flat mirror tilted to have a cut off energy of 22–25 keV was used to eliminate harmonics in the fully tuned mode for the Zr measurements. Sn K edge spectra were obtained similarly, except that the mirror was removed and the harmonic eliminated by detuning the angle θ between the two monochromator crystals so that the current in the ion chamber was half the maximum. The monochromator was calibrated by measuring the absorbance of a Zr/Sn foil between the scans of the samples. The first inflection point of this spectrum was defined as 17 999.35 eV for Zr and 29 199 eV for Sn. The corresponding ionization thresholds (E_0) were defined as 18 000 eV and 29 200 eV.

3.3. Muon spectroscopy

The present MuSR measurements were performed at the Swiss Muon Source (SμS) of the Paul Scherrer Institute, Villigen (Switzerland). Muon (μ^+) production is performed via pion production by targeting the proton beam on a carbon target. The muon is implanted into the sample, where it thermalises in about 2 ps, and then diffuses as a muon prior to its decay yielding a positron that is detected. After $\sim 10^7$ muons have been observed, the obtained time histogram result in a sinusoidal combined on an exponential decay. Due to the extremely weak muon depolarisation rate, the MuSR measurements were performed on the GPS instrument located in the πM3.2 beam-line. Due to the small depolarisation rate observed, the so-called muon on request (MORE) setup [15] was used. This setup dramatically reduces the B_g values and allows to extending MuSR time window up to 20 μs and therefore detecting polarisation rates as low as 1 kHz. Measurements were performed on in a transverse-field (TF – WEP magnet) of 50 Gauss. Detectors, forward, backward, up and down were used for the data analysis. Samples were cryo-cooled in liquid helium and MuSR was performed as a function of temperature between 5 and 300 K.

4. Results

4.1. X-ray penetration and X-ray absorption spectroscopy

The X-ray penetration through Zircaloy (density 6.5 g cm^{-3}) can be estimated using the absorption

data for an intensity attenuation of a factor e. For photons of 18.1 keV energy, i.e., above the Zr K edge, the penetration depth is 16.4 μm. For photon energy of 29.2 keV, i.e., above the Sn K edge, the penetration depth (e attenuation) is 40.1 μm. This allows to performing EXAFS analysis at these depths since the emitted photon of similar energy has to be originated from that depth.

Second-order polynomials were fit through both the pre-edge region below the absorption edge and the post-edge region above it to mimic the smooth backgrounds. The spectrum was offset to set the value of the extrapolated pre-edge polynomial to zero at 18020 eV and 29215 eV. The spectra were normalized by scaling them to set the value of the extrapolated post-edge polynomial to unity at these same energies. The extended fine structure was separated from the spectra by approximating the smooth, atomic background with a cubic polynomial spline, with the knot positions adjusted to minimize the area of the modulus of the Fourier transform of the k^2-weighted EXAFS below $R = 1.5$ Å. Fourier transforms were always calculated after the application of a sine window function to the EXAFS. Metrical parameters were obtained from the EXAFS weighted by k^2 via nonlinear, least-squares k-space curve-fits using the standard, harmonic EXAFS equation summed over shells and amplitudes and phases obtained from the FEFF7 code [16] and the hcp Zr crystal structure. It was assumed and subsequently corroborated by the data and curve-fits that the Sn substitutes for Zr with only minor distortions to the Zr site and that there is no clustering of the Sn that would result in significant numbers of Sn–Sn atom pairs so that only Zr neighbors were used in fitting both the Zr and Sn spectra. The fitting ranges for both Zr and Sn were $k = 3.1$–15 Å^{-1} and $R = 3.2$–6.5 Å, corresponding to the first six shells of the crystal structure, merging shells with less than 0.1 Å separation. Seven shells of neighbor atoms were used in the fits of the Zr spectra and six shells for Sn, floating the distances, numbers of atoms, and Debye–Waller factors. The number of independent parameters for these fitting ranges is 38 [17], substantially greater than the actual number used especially when taking into consideration that many of the floating parameters were constrained to certain ranges either independently or with respect to other ones. The third shell of the hcp structure with only two atoms could only be found if the number of atoms was fixed at two because of its small contribution to the overall fit. The ΔE_0's were fixed at values obtained by averaging the results from fits of the spectra in which ΔE_0 was allowed to float. The S_0^2 parameters were set at 0.25 for Zr and 0.98 for Sn using the criterion of twelve nearest neighbors from the spectrum of the recrystallised, undeformed sample. The self-absorption correction for the Zr is therefore included in the scale factor of the fit. In addition, since all samples were opaque and the correction identical all the relative changes between the spectra are unaffected by the self-absorbance and the S_0^2 simply a means for renormalizing the numbers of atoms to a more physically reasonable value. The phases of the data in k and the moduli and real parts of the transforms in R were compared with those of the fits for each shell to evaluate the level of confidence in these assignments. Errors were obtained by calculating the least squares error to the fit with and without the wave from a particular shell to determine its overall improvement in the quality of the fit. The floating parameters were then varied until the quality of the fit was worse by 10% of this contribution.

The Zr K $\chi(R)$ spectra (Fig. 1) of the samples with 0–100% elongation and the calculated spectra using the same 0.25 amplitude reduction factor as in the fits show the monotonic reduction in the amplitude of the nearest neighbour peak (Fig. 1, upper inset) that is expected if the strain increases the atomic scale disorder. The effect is, however,

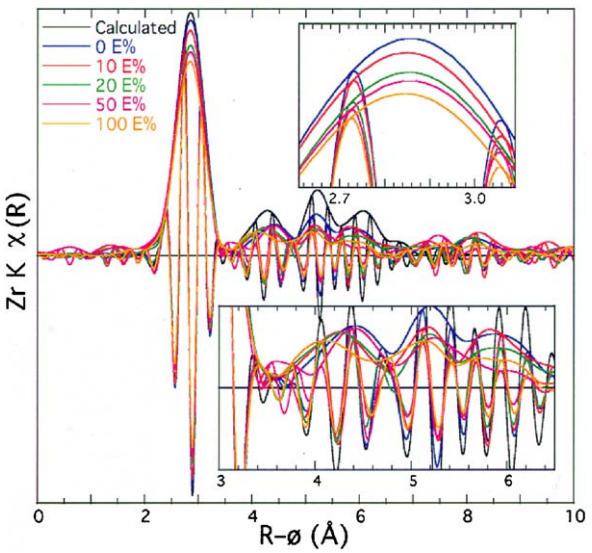

Fig. 1. Zr EXAFS data obtained for the 5 Zry2 samples as well as that calculated for the crystallographic structure the phase correction is 0.5 Å.

not a large one, the 20–25% diminution in the peak height results from a more modest increase in the Debye–Waller factor. The nodes of the real components of all of the spectra and the calculation overlay exactly through this region, indicating that no shifts in the nearest neighbour distances have occurred. Larger effects are observed in the extended region that contains the contributions of the more extended local environment through the fifth crystallographic near neighbour shell. Although the trend with bulk elongation is not as clear as for the first neighbour shell contribution because of some noise in the data, it is nevertheless evident that larger amounts of strain are associated with a loss of transform modulus amplitude that is 50% or greater at longer distances in the samples with the greater strains. This is consistent with non-specific disorder that increases with distance from the absorber. This tendency towards glassy behaviour is also demonstrated by the observation that the loss of amplitude results in only minor or negligible shifts in the nodes of the real components of both the samples (Fig. 1, lower inset) and the spectrum calculated from the crystal structure. Instead of aggregating at specific distances to form new shells, the atoms that are displaced from their lattice points by the strain are distributed so broadly that their contributions to the EXAFS are lost because of the destructive interference between their individual waves. The structure of the locally ordered fraction of the material continues to match that of crystalline Zr even when its overall length has doubled.

The exception is the region $R = 3.5$–4.5 Å. Although again not totally consistent with the extent of elongation, it is clear that larger deformations are associated with a shift of the modulus peak to lower R concomitant with a change in the pattern exhibited by the real component. This behaviour is most likely reflects the creation of an ordered shell of atoms not found in the crystal structure that results from a specific, stable, strain-induced inhomogeneity.

To first order the Sn spectra (Fig. 2) show the same pattern as the Zr of large near neighbour peak followed by three lower amplitude peaks out to around $R = 6.5$ Å. This result demonstrates that the Sn substitutes into a crystallographic Zr site with relatively little distortion of its local environment. The nearest neighbour contribution also decreases with increasing deformation of the samples. However, the relatively even, continuous

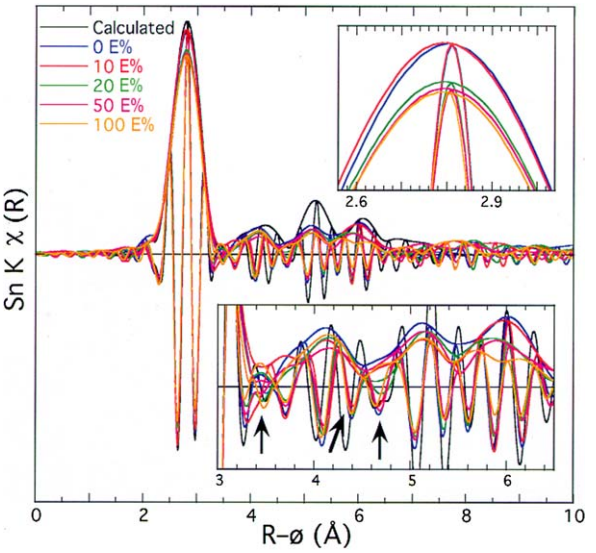

Fig. 2. Sn EXAFS data obtained for the 5 Zry2 samples as well as that calculated for the crystallographic structure the phase correction is 0.5 Å.

change observed for Zr is not duplicated for Sn. The spectra of the non-deformed 10% elongated sample exhibits the same amplitude as the recrystallised specimen, followed by around a 13% diminution for 20%, 50%, and 100% elongation (Fig. 2, upper inset). The nearest neighbour contributions in the Sn spectra therefore display only two amplitudes rather than a continuum. The decrease of the amplitude with elongation relative to the unstrained material in the extended region (Fig. 2, lower inset) also continues to be less than that of the Zr, implying that the Sn renders its local environment stiffer and more resistant to disorder than the Zr. Nor do the Sn spectra show the shift of the $R = 4.1$ Å modulus peak that was interpreted as the growth of a new shell associated with the strain-induced defects. However, the Sn spectra do show much larger shifts in the nodes of the real component in the $R = 3.8$–4.8 Å region relative to the spectrum calculated from the crystal structure and, at $R = 4.7$ Å, each other (arrows in Fig. 2, lower inset). Analogous to the Zr spectra, at longer R and over the nearest neighbour region the real component nodes remain close to those of the calculated spectrum. There are therefore some differences relative to the Zr in both the static structure of the Sn site and its response to the strain of the bulk elongation. These differences include the dependence of the response to the amount of strain as well as some of the details of the structure of the local

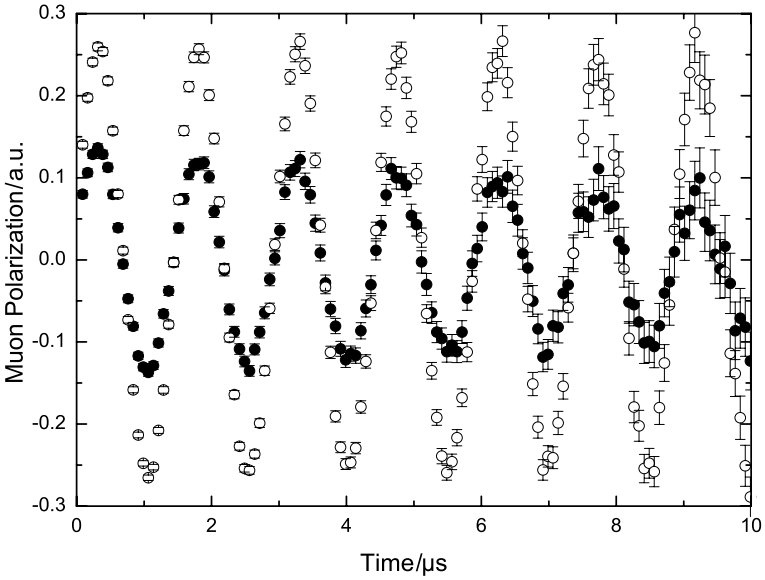

Fig. 3. The transverse-field (50 Gauss) MuSR spectra over 10 μs, in Zry2 at low temperature ($T = 5$ K). Legend: open symbol (○) for $\varepsilon = 0$ and solid symbol (●) for $\varepsilon = 100\%$. Note, prompt muonium formation could not be evidenced in the deformed sample.

environment around both the Zr and the substitutional Sn.

The most incisive method for determining changes in a solid solution first shell numbers and harmonic widths is by direct comparison and ratioing of the amplitude envelopes of this wave in $\chi(k)$. An overall reduction implies a reduction in the average number of atoms in this shell, a larger reduction at high k is indicative of an increase in the width of the static component of the distribution. Clearly in Fig. 1, the maxima of the amplitudes are in phase opposition with the imaginary sinusoidal signals that confirm that the next neighbours of Zr are Zr [9]. In Fig. 2 the Sn next neighbours are Zr and the amplitude maximum coincide with the maximum of the imaginary sinusoidal signal. On the other hand the amplitudes of the first shell reduced with the strain, but variation becomes more subtle for the other shells.

4.2. Muon Implantation and muon spectroscopy

Muon penetration through and implantation in Zircaloy (density 6.5 g cm^{-3}) was modelled using SRIM.2000 [18]. First calculations were carried out for an incident energy of 4 MeV. The average penetration depth for the μ^+ is 344 μm with a straggle of 23 μm and the damage density is insignificant. In this range only electronic interactions occur during the stopping process.

The transverse-field time spectra for muons in zirconium at low temperature ($T = 4$ K) were recorded for both unworked and worked samples (for typical MuSR spectra see Fig. 3). For the unworked sample, no muons forming muonium are detected and the totality of the muons is in a diamagnetic state, as evidenced by the amplitude of the observed signal. For the deformed sample, the amplitude of the worked sample is a factor two times smaller than that of the unworked sample. Measurements performed in very low transverse field could not reveal the presence of prompt muonium formation. The important loss of amplitude can tentatively be ascribed to muons stopping in the numerous grain boundaries, where delayed muonium formation could possibly occur.

The depolarization of the MuSR signal [i.e., the envelope $g(t)$] which is related to the possible muon diffusion was studied from 5 K to room temperature.

These data were recorded as a function of T in the range 5 K to room temperature. The relaxation was studied in the temperature range 5–273 K. The comparison of relaxation data for re-crystallised and cold-worked samples is given in the discussion.

5. Discussion

It is interesting comparing the EXAFS data obtained so far from the Zr and Sn edges. The Zr

Table 2
Comparison of crystallographic data with re-crystallised and cold-worked EXAFS data of Zr and Sn

Crystallographic R (pm)	N (–)	Zr EXAFS R (pm)	N (–)	σ (Å)	Sn EXAFS R (pm)	N (–)	σ (Å)
318	6	320 ± 2	11.1 ± 1.1	0.071	317 ± 2	12.5 ± 1.3	0.076
323	6	357 ± 2	0.9 ± 0.2	0.061	–	–	–
453	6	455 ± 2	3.0 ± 0.5	0.066	461 ± 2	5.8 ± 0.7	0.085
515	2	512 ± 2	[2.0]	0.071	512 ± 2	[2.0]	0.067
557	12	556 ± 2	8.5 ± 1.5	0.067	553 ± 2	8.0 ± 1.5	0.066
559	6	–	–	–	–	–	–
608	12	612 ± 2	6.0 ± 1.2	0.061	610 ± 2	10.8 ± 1.5	0.070
646	6	644 ± 2	2.3 ± 0.5	0.061	646 ± 2	13.7 ± 2.0	0.107

±: Error estimate.

next neighbour number N is 6 at 318 pm and 6 at 323 pm forming an apparent Zr cluster [$ZrZr_{12}$] without Zr-vacancy, defect or distortion. Since the precision on R is 2 pm, it is difficult to discriminate the 2 shells. Table 2 presents the results of the 8 first shells predicted and observed for Zr and Sn.

Although the re-crystallised material features correspond roughly to the crystallographic structure, disorder is indicated by the low amplitudes that are sensitive to N–σ correlations, the larger than normal errors (~10%). The slightly lower N number (11) for the Zr first shell may be due to twinning or Ω phase formation, these two first possibilities are unlikely. Further, the occurrence of 1 at.% Sn that is surrounded by 12 Zr next neighbour could yield 10% distortion, however, the Zr–Sn distance is 317 pm that may yield rather weak Zr–Zr bounding local extension. On the other hand, the presence of O also about at the at.% level may cause occasionally distortion or finally 10% inherent distortions due to defects may also be accounted for the extra Zr shell. The two latter hypotheses are supposed to be the most likely since post recrystallisation treatment may already induce some internal stresses and interstitial oxygen's induce displacements, e.g., [19]. A common feature in the residuals after fitting with the crystallographic shells implies the extra shell near 357 pm around Zr with one atom only.

The principal features of the Zr radial distribution function from the curve-fits of the Zr EXAFS are close to the crystallographic ones. Residual disorder results in the additional shell for 357 pm. On the other hand small shifts in the positions of some peaks, reduced amplitudes or some shells, and N–σ correlations that gives erroneously large numbers of atoms for others. The Sn–Zr nearest neighbour distance could be 3 pm lower than the Zr–Zr distance, however this difference is within the error of the measurement. Although the curve fits failed to identify any non-crystallographic shells, the disorder observed in the data is manifested in the more distant shells as significant shifts in the Sn–Zr distances, reduced amplitudes, and N–σ correlations that give erroneous large numbers of atoms.

It must be noted in Fig. 4 that the distortion of Zr persists what ever be the strain after cold rolling.

There is generally good correspondence between the primary features of the spectrum calculated from the crystal structure of Zr and both Zr and Sn experimental one. The exception is the region from 330 to 500 pm. The amplitudes diminish with cold rolling strain throughout the spectra, although the trend is less clear for the Sn than for the Zr spectra and the behaviour is complicated around 350 pm and 470 pm.

In MuSR, the depolarisation rate was studied as a function of the temperature. Muon trapping does not favourite generation of prompt muonium at 4–6 K. However, even in the re-crystallised Zry2 muonium is not detected. This may be due to the residual distortion, or because its occurrence lies below the detection limit ~2%.

For both sample, the depolarisation rate of the MuSR signal plotted versus temperature exhibits a clear decrease above 100 K (see Fig. 5). At low temperatures, the extremely weak value of the muon depolarization rate in the unworked sample is related to the fact that the field distribution sensed by the muon is solely given by the nuclear magnetic moments, i.e., only by the atom ^{91}Zr, which abundance is relatively low (11.2%). Above 100 K, the observed decrease reflects the occurrence of muon diffusion, as it will create a so-called motional-narrowing effect of the field distribution sensed by the implanted muon. As said above the MuSR signal for the worked sample exhibits reduced amplitude. This is ascribed to muons stopping in the high

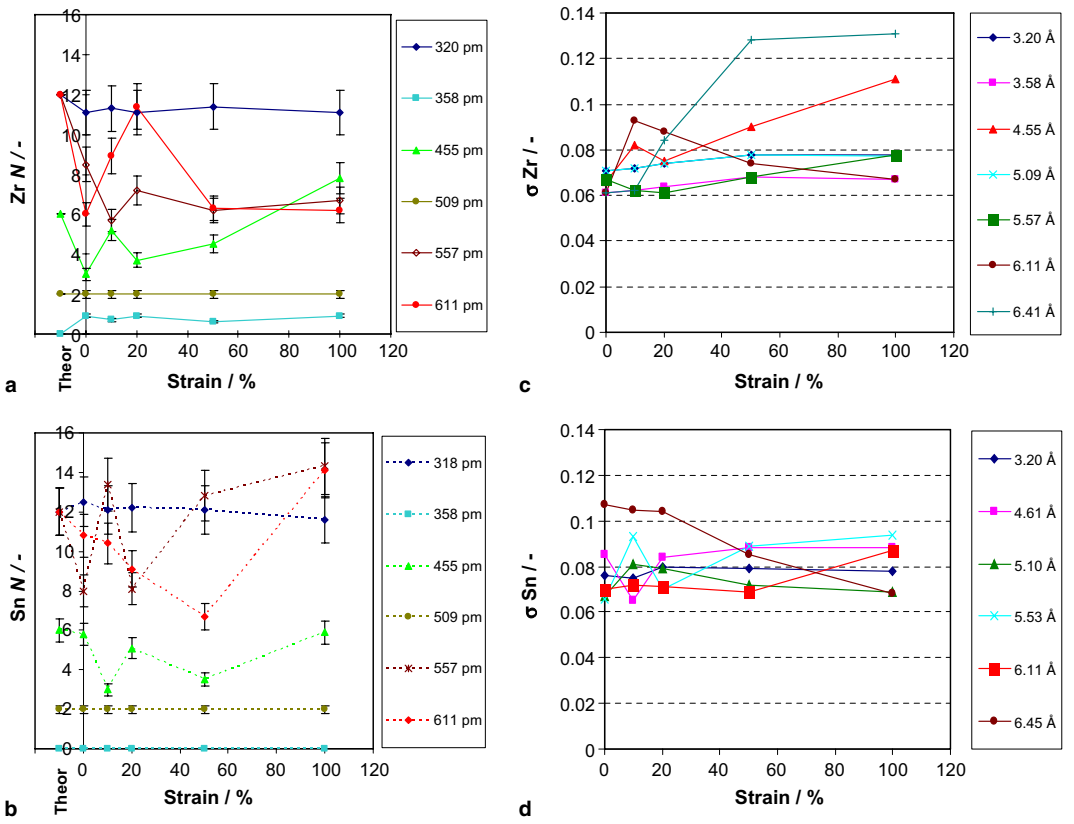

Fig. 4. Shell population (N) for Zr (a) and Sn (b) and Debye–Waller coefficient (σ) for Zr (c) and Sn (d) as a function of sample strain (%). Note the theoretical data for pure α-Zr is added for comparison, the 6 shell symbols are given for increasing distance in pm.

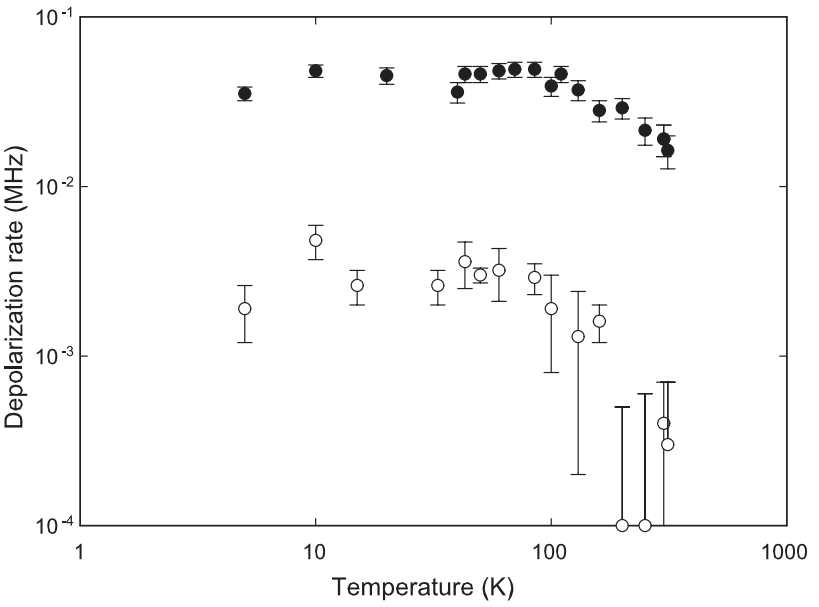

Fig. 5. Temperature evolution of the MuSR depolarisation rates (λ) obtained in weak transverse-field (50 G) for re-crystallised Zry2 (○) and for 100% strain (●) (see also text).

density of grain boundaries, where the large disorder creates an extremely fast muon depolarization not detectable by the detector electronics. The rest of the signal is due to muons stopping in the nanophase crystals. As observed, even this signal exhibits a larger depolarization in which the disorder is larger.

6. Concluding remarks

The first goal of this study was to understand how defects due to strain propagate through Zry2 at the sub-nanoscopic level when it increases. The investigations were performed successfully by extended X-ray absorption fine structure (EXAFS) spectroscopy and by muon spin relaxation (MuSR) analysis. The EXAFS revealed the population of the shells over more than 650 pm and were quantified as a function of cold rolling strain in the samples. EXAFS showed a subtle variation of number neighbour as a function of strain for the third, fifth and sixth shells. Results obtained by MuSR are compatible with a much higher density of grains boundaries in the worked sample and, in agreement with EXAFS, with a higher degree of disorder in the nanophase crystal.

Acknowledgements

The MuSR work was performed at the Swiss Muon Source (SμS) of the Paul Scherrer Institute (PSI), Villigen, Switzerland and the X-ray absorption tests were carried out at the Stanford Synchrotron Radiation Laboratory (SSRL). The authors thank both organisations for the access and support of the beam lines. Acknowledgements are due to Swiss Nuclear for its financial support of the LWV where part of the work was performed. The authors thank W. Hoffelner and U. Zimmerman (PSI) for their interest in their work.

References

[1] F. Foskolos, W. Kröger, Scientific Annual report 2001, vol. 4, Nuclear energy and safety, overview of the main activities, Paul Scherrer Institute, 2002.
[2] G. Aurelio, A. Fernández Guillermet, J. Alloys Comp. 298 (2000) 30.
[3] G.P. Dinda, H. Rösner, G. Wilde, Scr. Mater. 52 (2005) 577.
[4] M. Kiran Kumar, I. Samajdar, N. Venkatramani, G.K. Dey, R. Tewari, D. Srivastava, S. Banerjee, Acta Mater. 51 (2003) 625.
[5] K. Kapoor, D. Lahiri, C. Padmaprabu, T. Sanyal, J. Nucl. Mater. 303 (2002) 147.
[6] M. Matsuura, M. Sakurai, K. Amiya, A. Inoue, J. Alloys Comp. 353 (2003) 240.
[7] V.G. Storchak, J.H. Brewer, S.F.J. Cox, J. Low Temp. Phys. 111 (1998) 303.
[8] M. Borghini, T.O. Niinikoski, J.C. Soulié, O. Hartmann, E. Karlsson, L.O. Norlin, K. Pernestål, K.W. Kehr, D. Richter, E. Walker, Phys. Rev. Lett. 40 (1978) 1723.
[9] B.K. Teo, EXAFS: Basic Principles and Data Analysis, in: C.K. Jorgensen, S.J. Lippard, K. Niedenzu, R.W. Parry (Eds.), Inorganic Chemistry Concepts, vol. 9, Springer-Verlag, New York, 1986, p. 349.
[10] S.J. Blundell, Contemporary Physics 40 (1999) 175.
[11] V.G. Storchak, J.H. Brewer, S.F.J. Cox, J. Low Temp. Phys. 111 (1998) 303.
[12] T.R. Waite, Phys. Rev. 107 (1957) 463.
[13] G. Storchak, N.V. Prokof'ev, Rev. Mod. Phys. 70 (1998) 929.
[14] J.R. Bargar, G.E. Brown Jr, I. Evans, M. Rowen, T. Rabedeau, J.H. Rogers, The hard X-ray spectroscopy molecular environmental sciences beam line at SSRL, in: T.B. Reich, D.K. Shuh (Eds.), Speciation Techniques and Facilities for Radioactive Materials at Synchrotron Light Sources, Nuclear Energy Agency, OECD, 2001, p. 169.
[15] R. Abela, A. Amato, C. Baines, X. Donath, R. Erne, D.C. Gorge, D. Herlach, G. Irminger, I.D. Reid, D. Renker, G. Solt, D. Suhi, M. Werner, U. Zimmermann, Hyperfine Interact. 120&121 (1999) 575.
[16] A.L. Ankudinov, J.J. Rehr, Phys. Rev. B 56 (1997) R1712.
[17] E.A. Stern, Phys. Rev. B 48 (1993) 9825.
[18] J.F. Ziegler, J.P. Biesack, U. Littmark, The stopping range of ions in solids, Pergamon, New York, 1985.
[19] M.S. Blanter, E.B. Granovskiy, L.B. Malagas, Mater. Sci. Eng. A 370 (2004) 88.